Type III Secretion Effector VopQ of *Vibrio parahaemolyticus* Modulates Epithelial Cells' Central Carbon Metabolism

Nguyen Quoc Anh[a,b], Takaaki Shimohata[a#], Sho Hatayama[a], Aya Tentaku[a], Junko Kido[a], Thi Mai Huong Bui[b], Takashi Uebanso[a], Kazuaki Mawatari[a], Akira Takahashi[a]

[a] Department of Preventive Environment and Nutrition, Institute of Biomedical Sciences, Tokushima University Graduate School

[b] Department of Food Microbiology and Molecular Biology, National Institute of Nutrition, 48 B Tang Bat Ho, Hanoi, Vietnam

Corresponding author: Takaaki Shimohata shimohata@tokushima-u.ac.jp

Running title: *V. parahaemolyticus* effector modulates host metabolism

Abstract word count: 257 words

Main text word count: 4400 words

Keywords: Metabolomics, host-pathogen interaction, *Vibrio parahaemolyticus,* T3SS effector,

ABSTRACT

Vibrio parahaemolyticus is a Gram-negative halophilic pathogen that frequently causing acute gastroenteritis and occasional wound infection. *V. parahaemolyticus* contains several virulent factors, including Type III secretion systems (T3SSs) and thermostable direct hemolysin (TDH). In particular, T3SS1 is a potent cytotoxic inducer, and T3SS2 is essential for causing acute gastroenteritis. Although much is known about *V. parahaemolyticus*'s effector manipulating host signaling transductions, little is known about the host metabolomic changes modulated by *V. parahaemolyticus*. To address this knowledge gap, we performed a metabolomic analysis of the epithelial cells during *V. parahaemolyticus* infection using capillary electrophoresis–time-of-flight mass spectrometry (CE-TOF/MS). Our results revealed significant metabolomic perturbations upon *V. parahaemolyticus* infection. Moreover, we identified that T3SS1's VopQ effector was responsible for inducing the significant metabolic changes in the infected cells. The VopQ effector dramatically altered the host cell's glycolytic, tricarboxylic acid cycle (TCA), amino acid metabolisms. VopQ effector disrupted host cell redox homeostasis by depleting cellular glutathione and subsequently increasing the level of reactive oxygen species (ROS) production.

IMPORTANCE

Metabolic response of host cells upon infection is pathogen - specific, and the infection-induced host metabolic reprogramming may have beneficial effects on the proliferation of pathogens. *V. parahaemolyticus* contains a range of virulent factors to manipulate host signaling pathways and metabolic processes. In this study, we identified that T3SS1's VopQ effector rewrites host metabolism in conjunction with the inflammation and cell death processes. Understanding how

VopQ reprograms host cell metabolism during the infection could help us to identify novel therapeutic strategies to enhance the survival of host cells during *V. parahaemolyticus* infection.

Introduction

Vibrio parahaemolyticus is an aquatic Gram-negative bacterium and the causative agent of the acute gastroenteritis associated with the ingestion of raw seafood and water. Occasionally, *V. parahaemolyticus* causes wound infection and septicemia in immunocompromised individuals (1, 2). The pandemic strains of *V. parahaemolyticus* are an important public health concern, and climate change is linked to the increased incidence of *V. parahaemolyticus* outbreaks worldwide (3, 4). Clinical isolates of *V. parahaemolyticus* contain numerous virulent factors, including pore-forming thermostable direct hemolysin (TDH) toxin and two Type III secretion systems (T3SSs) that enable the delivery of bacterial effectors into the eukaryotic host (5, 6).

The T3SS1 is located in an ancestral region to the bacterial first chromosome and presented in both non-pathogenic and pathogenic strains. The T3SS2 encoded genes are located on the pathogenicity islands (Vp-PAI) in the second chromosome and are associated with infectious diarrhea in humans. (7, 8, 9). T3SS1 is cytotoxic in mammalian cells, yeast and cause mortality in murine peritoneal and pulmonary infection models, whereas T3SS2 is necessary for in vivo enterotoxicity in the infant rabbit infection and mouse models (10, 11, 12, 13).

To date, four effectors of T3SS1 have been identified (14, 15). In particular, the VopQ effector (VP1680 or VepA) effector has been extensively studied and is found both necessary and sufficient to induce a non-apoptotic form of cell death in vitro (16). VopQ provokes inflammatory responses through the MAPK/ERK pathway, leading to IL-8 secretion in infected Caco-2 cells (17, 18). VopQ activates NLRC3 inflammasome complexes (NOD-like receptor CARD domain-containing 3) but interferes with the activation of NLRC4 (NOD-like receptor

CARD domain-containing 4) inflammasomes in bone marrow-derived macrophages (19). Biochemical studies showed that VopQ effector disrupts lysosomal proton gradients by interacting with Vo domain of vacuolar H+-ATPase (v-ATPase) and forming an outward rectifying pores in lysosomal membrane, thus causing the release of small molecules (< 3 kDa) from the lysosomal lumen (20, 21). Consequently, VopQ inhibits host autophagic flux by preventing lysosomal acidification and membrane fusion (22). Recently, transcriptome analysis revealed that T3SS1 activates pro-survival and suppresses cell death networks in infected human fibroblasts (23)

Metabolomics, as an emerging analytical platform, has been applied to decipher host physiological perturbation and identify altered metabolic pathways during bacterial infections (24, 25). In this study, we investigated the dynamics of the metabolic processes of the epithelial cells during *V. parahaemolyticus* infection and the role of T3SS1's VopQ effector in modulating host cell metabolism using capillary electrophoresis–time-of-flight mass spectrometry (CE-TOF/MS). Herein, we identify that T3SS1's cytotoxic VopQ effector is a metabolic disruptor, profoundly altering host metabolisms.

Result

V. parahaemolyticus infection-induced distinct metabolome alteration in the infected host cell

Clinically isolated *V. parahaemolyticus* contains three principal identified virulent factors, including TDH toxin, and Type III secretion systems 1 (T3SS1) and Type III secretion systems 2 (T3SS2), located in bacterial chromosomes 1 and 2, respectively (7). To study the metabolomic responses of the human adenocarcinoma epithelial cell line Caco-2 to *V. parahaemolyticus's* virulent factors, we infected Caco-2 cells with several *V. parahaemolyticus* mutant strains carrying specific virulent factors. The ΔvscN1-ΔvscN2 mutant strain derived from the clinical isolate RIMD2210633 contains double deletion for genes for ΔvscN1and ΔvscN1, which are encoding structural components of the T3SS1 and T3SS2 secretion apparatus respectively. Similarly, POR2 and POR3 derived from parental POR1 strain contain double genetic deletions of *tdhAS* and have a deletion of *vcrD1* (T3SS1) and *vcrD2* (T3SS2) respectively, which encode the inner membrane structural ring for T3SS apparatus. The resulting mutant strains, ΔvscN1-ΔvscN2 (ΔT3SS1, ΔT3SS2), POR2 (ΔTDH, ΔT3SS1), and POR3 (ΔTDH, ΔT3SS2), POR4 (ΔTDH, ΔT3SS1, ΔT3SS2) were used in our first metabolomic analysis to assess their impacts on the infected Caco-2 cell's metabolomes. The bacterial strains and phenotypic descriptions used in this study were summarized in Table 1 and Table 2.

The infections were performed at a multiplicity of 50 bacterial cells per infecting Caco-2 cell to ensure full exposure of the infected cell population, and the total metabolome was extracted at 120 min post-infection to avoid excessive cytotoxicity causing leakages of cellular metabolites (Fig. S1 in the supplemental material). CE-TOF/MS identified 87 metabolites matching with the validated standards, and the changes in the relative levels of quantified metabolites upon the infections were visualized by heatmap hierarchical clustering, shown in Fig. 1A. Principal component analysis (PCA) (Fig. 1B) was performed to demonstrate further the distinct clusters of metabolites in the different infection groups. The combination of three components shown cumulatively explain 69.7% of the variation in the metabolite dataset.

To determine which host biochemical pathways were significantly altered by *V. parahaemolyticus* infection, we performed functional metabolite set enrichment analysis (MSEA) to identify overrepresented metabolites in the cells infected *V. parahaemolyticus* wildtype compared to the control group (sham infection) with human metabolite's libraries databases using MetaboAnalyst Suite 4.0 (26). The MSEA analysis was presented according to the scores from enrichment analysis (y-axis) and topology analysis (x-axis) (Fig. 1C). The infection of Caco-2 cell with *V. parahaemolyticus* resulted in drastic changes in the multiple metabolites involved in glycolysis and its associated pathways, amino acid and nucleotide metabolism, and the TCA cycle metabolites (Fig. 1C). Overall, the metabolomic response to *V. parahaemolyticus* infection showed a strong correlation with the presence of the T3SS1 virulent factor (POR3 and WT), and the metabolic profiles of cells infected with POR4, POR2, or ΔvscN1–ΔvscN2 strains were more correlated with the control group. Consequently, although there was the divergence in metabolomes of cells infected with POR4, ΔvscN1–ΔvscN2, and POR2 in the comparisons with the control group (sham infection) (Fig. 1B), in the context of metabolic analysis, it appeared that T3SS1 contributed the most significant metabolic perturbation observed in the infected Caco-2 cells.

VopQ, a T3SS1 effector, rewrites host cell metabolomes

T3SS1 translocates four identified protein effectors, including VopQ (VP1680), VopR (VP1683), VopS (VP1686), and VPA0450, working in tandem to induce autophagosome accumulation, plasma membrane blebbing, cell rounding, and eventually cell death (17, 18). Since VopQ is known to induce cell cytotoxicity and lysosomal dysfunctions, we hypothesized that VopQ is a metabolic modifier of T3SS1 that underlies the host metabolic perturbation. Next, we constructed a *V. parahaemolyticus* ET4 strain derived from the parental POR3 strain, which contained only a single VopQ effector (ΔVP1683, ΔVP1686, and ΔVPA0450) and S1-ENM, a V. parahaemolyticus T3SS1 effector-deficient strain (ΔVP1680, ΔVP1683, ΔVP1686 and Δ VPA0450).

We performed a metabolomic analysis of Caco-2 cells infected with VopQ^{+} strains (POR3 and ET4), and S1-ENM, a VopQ deficient strain. We observed the profound metabolomic alterations at 90 post-infection in the cells infected with the $\mathrm{T3SS1}^{+}$ strain (POR3 and ET4) (Figure 2A). In particular, Principal component analysis (PCA) showed clear discrimination between Caco-2 cells infected with the ET4 and POR3-infected cells, compared to the control (sham infection) and S1-ENM strain-infected cells. The combination of three components shown cumulatively explain 71.3 % of the variation in the metabolite dataset (Fig. 2B). Also, hierarchical cluster analysis of the infection group's metabolite data set by Euclidean distance showed two distinct clusters I (S1-ENM and Control) and II (POR3 and ET4) (Fig. 2C). Thus, our result suggests that the T3SS1's VopQ was responsible for the host metabolic change in Caco-2 infection model.

Additionally, to monitor the onset of metabolomic changes during the infection, we performed a time-series analysis of Caco-2 cells infected with ET4 and S1-ENM strains. We observed progressively metabolomic alterations starting from 90-minutes but not initial 45-minutes post-infection in ET4 strain infected cells compared to the control and S1-ENM (Fig. S2 in the supplemental material).To further confirm these results, , we analyzed the metabolomes of Human cervix carcinoma INT-407 (a HeLa derivative) cell line infected with ET4 and S1-ENM strains. Consistent with the previous metabolomic analysis results in Caco-2 cells, ET4 induced a significant metabolomic change in INT-407 cells, and VopQ effector-deficient strain, S1-ENM, showed a metabolic pattern similar to that of the control (Fig. S3 in the supplemental material).

<u>*VopQ effector repressed host cell energy metabolism*</u>

Among the metabolites that were determined by the CE-TOF analytical system, we observed two to threefold increased levels of the upper glycolytic intermediates such as glucose 6-phosphate (G6P) and fructose 6-phosphate (F6P) in Caco-2 cells infected by *V. parahaemolyticus* POR3 and ET4 strains but not with the S1-ENM strain at 90 min post-infection ($p < 0.05$) (Fig. 3). Interestingly, the levels of subsequent downstream glycolytic intermediates were altered in Caco-2 cells infected with ET4 or POR3 compared to S1-ENM and the control. In ET4 and POR3, we found significant reductions of downstream glycolytic intermediates, including fructose 1,6-phosphate (F-1,6-P), 3-phosphoglycerate (3GP), phospho(enol)pyruvic acid (PEP), and pyruvic acid (PYR) ($p < 0.05$) (Fig. 3), compared to Caco-2 cells infected with the S1-ENM mutant or with the control. However, we were unable to detect glyceraldehyde 3-phosphate and 2-phosphoglycerate, perhaps because of their high turnover or low stability. Also, the end product of glycolysis, lactate, was lower in ET4 and POR3-infected cells compared to infection with S1-ENM or the control ($p < 0.05$). These data suggested that *V. parahaemolyticus*'s VopQ effector halted glycolytic cycles in the infected cells.

The accumulation of the upper and the depletion of the lower glycolytic intermediates in Caco-2 cells infected with ET4 and POR3 strains implicated a bottleneck in glycolytic flux at the step catalyzed by enzyme phosphofructokinase-1 (PFK-1) that converted G6P to F-1,6-P. The accumulation of F6P and decreased downstream glycolytic metabolites in ET4 and POR3-

infected cells were correlated with the increased levels of pentose phosphate pathway (PPP) intermediates such as sedoheptulose-7-phosphate, which indicated a possible metabolic reroute from glycolysis to PPP. Since, Phosphofructokinase-1 (PFK-1), a tetramer that is encoded by PFK-M (muscle), PFK-L (liver), and PFK-P (platelets), functions as the gatekeeper to glycolysis by catalyzing the phosphorylation of F6P into F1,6-P, we determined whether VopQ directly inhibits cellular PFK-1 activity in infected Caco-2 cells by enzymatic assay (27). Unexpectedly, the PFK-1 activities of Caco-2 cells infected with POR3 and ET4 were equivalent to those of cells infected with S1-ENM, and the control indicated that VopQ indirectly inhibited PFK-1 function (Fig. S4 in the supplemental material).

We observed dramatic alterations of the TCA cycle's intermediary metabolism in the infected cells with VopQ^{+} strains (POR3 and ET4). Pyruvate, the end-product of glycolysis is converted to acetyl-CoA, was severely depleted in the infected cells with POR3 and ET4. Pyruvate contributes energy to the living cells by its conversion to acetyl-CoA, a primary fuel of the TCA cycle. Even though we observed a steeply decreased level of pyruvate, the level of acetyl-CoA was slightly reduced through it is not statistically significant in the POR3 and ET4 infected cells (Fig. 3). Moreover, the levels of citrate, isocitrate, and succinate increased, whereas the levels of malate, fumarate, and α-ketoglutarate decreased in cells infected with VopQ^{+} strains (Fig. 3). As citrate is a potent inhibitor of phosphofructokinase-1 and the intracellular accumulation of citrate can lead to the inhibition of glycolysis and the increase of F6P and G6P level, as seen in our result (Fig. 3) (27, 28). Expectedly, the cellular nucleoside triphosphates (ATP) were decreased in conjunction with a significantly increased level of nucleoside monophosphates (AMP) (Fig. 4A). To determine whether the deprivation of pyruvate is responsible for the depletion of cellular

ATP, we treated Caco-2 cells with Ethyl pyruvate (EP), a cell-permeable derivative of pyruvic acid that can be readily converted to acetyl-CoA (29). Ethyl pyruvate is an effective ROS scavenger with anti-inflammatory properties and cytoprotective (30). Administration of 5 mM (or 10 mM) ethyl pyruvate did not restore ATP level nor cytoprotective for $VopQ^+$ strain infected Caco-2 cells (Fig. S7 in the supplemental material). This limited result suggested that the deprivation of pyruvate per se unlikely contributes to the reduction of cellular ATP through the TCA cycle.

Since glycolysis and the oxidative phosphorylation are central ATP generating biochemical pathways in the cells. To examine the contribution of energy-generating pathways to the survival of Caco-2 cells during the infection, we pretreated Caco-2 cells with the glycolytic inhibitor 2-deoxy-D-glucose (2-DG) and with rotenone, a mitochondrial respiratory chain complex I inhibitor. The result showed that inhibition of glycolysis but not mitochondrial oxidative phosphorylation sensitized Caco-2 cells to VopQ mediated cell death (Figs. 4B and C). Furthermore, Caco-2 cells cultured in glucose-free Dulbecco's modified Eagle's medium (DMEM) one day after reaching confluency or Caco-2 cells cultured in galactose-DMEM (glucose-free), which is known to enhance oxidative phosphorylation but to reduce glycolytic flux, showed increased susceptibility to VopQ (31, 32) (Fig. S5 in the supplemental material). In summary, our data suggested that VopQ repressed cellular energy metabolisms in Caco-2 cells preceding the cellular destruction.

VopQ alters host intracellular amino acid and induced reactive oxygen species (ROS) production

Throughout *V. parahaemolyticus* infection, we observed significant changes in amino acid abundances in the infected cells, which were strongly associated with the presence of the VopQ effector. At 90 min post-infection, we also detected that VopQ induced increases in intracellular abundances of lysine and arginine but decreased glucogenic amino acids such as glycine, beta-alanine, serine, proline, aspartate, and the two essential amino acids tryptophan and threonine (Fig. 5A). The level of alanine, a principal metabolite of pyruvate metabolism principally produced via pyruvate transamination, was also markedly reduced in cells infected with $VopQ^{+}$ strains ($p < 0.05$) (Fig. 5A). In addition, our metabolomic analysis indicated that the level of cellular antioxidant glutathione but not glutathione disulfide was reduced in cells infected with the $VopQ^{+}$ effector strains compared to S1-ENM infections that lacked VopQ. The complementation of the VopQ gene on a plasmid restored the reduced glutathione (GSH)-depleting phenotype of S1-ENM (Fig. 5B and 5C). This result indicated that the VopQ effector was necessary and sufficient to deplete the epithelial cell's GSH pool. Indeed, VopQ-induced reduction of GSH was accompanied by a steep rise of cellular hydrogen peroxide (H_2O_2) and superoxide (O_2^{-}), measured by fluorescence spectroscopic assay (Figs. 5D and 5E).

Since glycine and cysteine availability is the rate-determining factor in GSH biosynthesis, we tested the hypothesis that the reduction of cytosol glycine and cysteine jointly determined the glutathione synthesis rates in infected cells. The supplement of glycine or cell-permeated *N*-acetylcysteine or both in the culture medium did not lead to the restoration of the total GSH content in ET4-strain-infected cells (Fig. S6 in the supplemental material). On the other hand, there was no GSH detected in the culture medium during the infection, indicating that GSH efflux was unlikely to be responsible for the depletion of GSH content. Taken together, our results suggested that VopQ-induced GSH depletion and subsequently increased level of reactive oxygen species (ROS) in infected cells were independent of the variation of glycine and cysteine.

Discussion

In this study, we explored the metabolomic landscape of epithelial cells infected with *V. parahaemolyticus*. We determined that a bacterial T3SS1 effector, VopQ induces a widespread metabolic perturbation in the infected cells, profoundly altering host central carbon metabolism and amino acid metabolism. During *V. parahaemolyticus* infection, VopQ inhibits the activation of the host NLRC4 inflammasome but triggers the assembly of NLRC3 inflammasomes by activating caspase-1 processing of pro-IL-1b and pro-IL-18 and eventually the secretion of proinflammatory cytokines (19). Cellular metabolism plays a central role in regulating immune responses and inflammation in immune cells (33, 34). Several studies have suggested that inflammasome activation is modulated by several glycolytic enzymes (35). For example, inhibiting hexokinase-1 or pyruvate kinase (PKM2) suppresses NLRP3 inflammasome activation in macrophages (36, 37). While other studies reported inhibition of the glycolytic enzymes by 2-deoxyglucose (2 - DG) treatment, glyceraldehyde 3-phosphate dehydrogenase (GAPDH) and α-enolase can trigger NLRP3 inflammasome activation (38, 39). These contracting results illustrate the mechanistic complexity and plasticity of cellular metabolism. In *Salmonella*-infected macrophages, cellular glycolysis is diminished because of the uptake of host cell glucose by *Salmonella* in conjunction with SPI-1 T3SS-dependent NLRP3 activation (40). Mechanistically, *Salmonella typhimurium* mutant strain lacking the TCA enzyme aconitase induced rapid NLRP3 inflammasome activation by inducing bacterium-derived citrate accumulation, leading to the upstream accumulation of F6P and G6P (40). Our results implicated that the VopQ-mediated inhibition of host cell glycolysis may be linked to the activation of NLRC3 inflammasomes in macrophages (19). In addition, our results showed that the decrease in glycolysis flux increased the sensitivity to VopQ-mediated cell death. These findings suggest that VopQ effector interfering with cellular energy metabolism and the survival of the host cells.

Cells infected with VopQ showed decreased amino acid metabolism, including several nonessential amino acids and some metabolites involved in the anabolic pathways of these amino acids. Amino acids play a pivotal role in regulating physiology and cell proliferation. Consequently, the variation in cellular amino acid metabolism could substantially influence the outcome of an infection. Indeed, bacterial, parasitical, and viral infections have been associated with significant metabolic alterations in mammalian hosts (41, 42). For instance, enterotoxigenic *Escherichia coli* (ETEC) infection decreases isoleucine level in piglet serum and reduces the concentration of nonessential amino acids, including glutamine, asparagine, citrulline, and ornithine, but increases the levels of glycine and GABA (43). During invasive *Salmonella* or *Shigella* infections, the epithelial cell's intracellular amino acids were acutely depleted, leading to the inhibition of mTOR activity and the activation of autophagy (44). Indeed, VopQ is capable of rapidly induce autophagy in both phagocytic and non-phagocytic cells (19, 45).

The alteration of the intracellular amino acids induced by VopQ can be a result of changes in either amino acid metabolism or amino acid transport or both. Glycolysis and the TCA cycle both provide indispensable carbon skeletons, including 3-phosphoglyceric acid, pyruvic acid, and α-ketoglutarate, for the biosynthesis of nonessential amino acids. Through a cascade of enzymatic reactions, chiefly transaminases and aminotransferases, these carbon donors are converted into corresponding amino acids: serine, glycine, and cysteine (3-phosphoglyceric acid); alanine (pyruvic acid); and aspartic acid and glutamic acid (α-ketoglutarate) (46). Therefore, the de novo biosynthesis of amino acids strictly requires the availability of a carbon donor or a structurally related amino acid. The decreased level of nonessential amino acids in infection with $VopQ^+$ strains is consistent with the severe depletion of glycolytic and the TCA cycle's intermediates, namely, 3-phosphoglyceric acid, pyruvic acid, and α-ketoglutarate. Although we cannot exclude the possibility that VopQ can alter the rate of amino acid transport in the infected cells, it is likely that the reduction of nonessential amino acids induced by VopQ was due to a lack of carbon donor precursors.

Another important finding in our study is that VopQ depletes the host's cellular glutathione and induces oxidative stress. Glutathione is a tripeptide, consisting of glycine, cysteine, and glutamate that participates in many critical cellular functions in mammalian cells (47, 48). Glutathione is predominantly found in the cytosol mainly in the reduced state (GSH) and less often in its oxidized state, glutathione disulfide (GSSG). Together with other antioxidant enzymes, the GSH/GSSG redox system safeguards the cellular oxidative balance (49). GSH plays a major role in the removal of many reactive species such as superoxide (O_2^-) and hydrogen peroxide (H_2O_2) through GSH peroxidase oxidization of GSH to GSSG and H_2O. The depletion of GSH is a marker of a disease's associated pathological state and the development of destructive cellular processes such as apoptosis and necrosis (50).

Our study has several limitations. First, we measured the abundance of selected metabolites, and therefore, we only captured a metabolomic snapshot at a given time of sampling, but not the metabolic turnover rate, which represents the dynamic status of cellular biochemical processes. Consequently, we were unable to elucidate the exact metabolic flux of host cells' responses to *V.*

parahaemolyticus infection. Second, our study used Caco-2 and INT-407 cell lines, which are established cancer cell lines, as the infected host cells. Those cell lines are known to be metabolically altered to favor glycolytic metabolism over oxidative phosphorylation, even in the aerobic conditions. Thus, this inherent metabolic abnormality can mask pathogen-induced host interaction. Additional studies with other primary cells are warranted to confirm further the general relevance of these metabolomic patterns observed in Caco-2 cells. In summary, we identified that the *V. parahaemolyticus* VopQ effector subverted Caco-2 cells' energy metabolism, amino acid balance, and redox hemostasis. Boosting the cellular bioenergetic state can be a promising target to enhance cellular survival during *V. parahaemolyticus* infection.

Material and methods

Bacterial strains and culture conditions

V. parahaemolyticus strain RIMD2210633 (KP-positive, serotype O3: K6) was used as the standard strain. The bacteria were cultured in Luria–Bertani (LB) medium supplemented with 3% NaCl at 37°C. For the construction of deletion mutants, *Escherichia coli* DH5α and SM10λpir strains were used to mobilize plasmids into *V. parahaemolyticus*. *Escherichia coli* strains were cultured in LB medium supplemented with antibiotics at the following concentrations with shaking at 37°C: kanamycin, 50 μg mL^{-1}, and chloramphenicol, 20 μg mL^{-1}. Strains and constructed plasmids used in this study are presented in Table S1 in the supplemental material.

Construction of deletion mutants

Deletions of mutant strains were constructed by a two-step allelic exchange method using POR3 as the parental strain, as previously described (51). Briefly, approximately 400–500 nucleotide fragments of DNA regions upstream and downstream of the targeted gene were amplified by polymerase chain reaction (PCR) using the primers listed in Table S1 in the supplemental material. Primers 2 and 3 contained a 15–18 bp overlapped site to connect the 3’ end of the upstream fragment with the 5′ end of the downstream fragment. Two amplified DNA fragments were joint by the second round of overlapping PCR using primers 1 and 4. The amplified fragment was cloned into Blunt End TOPO Cloning (Thermo Fisher Scientific) and propagated in *E. coli* DH5α. The inserted fragment containing a deletion cassette was excised by restriction digestion with BamHI and PstI and subcloned into the suicide vector pYAK1. The constructed plasmid was introduced into *E. coli* strain SM10λpir and was mobilized into the *V. parahaemolyticus* POR3 strain by conjugation. The crossing-over colonies were selected by counterselection on 10% sucrose TCBS. Isolates with deletion allele were confirmed by PCR and sequencing.

Complementation of deleted genes

Complementation of deleted genes was carried out as previously described (51). Briefly, the VP1680 coding region of VopQ was amplified by PCR and was subsequently cloned into pSA19CP-MCS, and the plasmid construct was introduced into the deletion mutant strains by electroporation.

Cell culture

Caco-2 cells and INT-407 cells were cultured in DMEM (Sigma-Aldrich) supplemented with 10% fetal bovine serum (Gibco BRL) and 50 μg/mL gentamicin (Sigma-Aldrich). Caco-2 cells and INT-407 cells were seeded at 4×10^5 and 8×10^5 cells/well, respectively, in a 6-cm cell culture plate. The cells were maintained at 37°C in a humidified atmosphere of 5% CO_2. Caco-2 and INT-407 cells that were cultured for 4 and 3 days, respectively, were used for subsequent experiments.

Infection protocol

The culture medium was replaced with fresh DMEM (without supplements) at 2 hours before infection. For the first metabolomics analysis (result in figure 1), after overnight cultivation, bacteria were harvested by centrifugation at 6,000 rpm at room temperature and were resuspended in phosphate-buffered saline (PBS) and adjusted to an OD_{600} of 1.0. Bacteria were inoculated into the mammalian cells at a multiplicity of infection (MOI) of 50 bacterial cells to one Caco-2 cell (50:1), and the infections were allowed to proceed at 37°C in 5% CO_2 at each different time point.

For the second metabolomics analysis (result in Figure 2), to ensure the uniform expression of VP T3SS1, overnight cultured bacteria were inoculated in DMEM in a humidified atmosphere containing 5% CO_2 at 37°C for 6 h before starting the experiment. Other subsequent steps were the same as described in the above text.

Metabolite extraction and CE-TOF/MS analysis

Cells were collected for metabolome analysis at indicated infection times. Approximately 2.5×10^6 cells were infected with each *V. parahaemolyticus* strain at each given time point, with MOI 50:1. The supernatant was removed, and cells were washed twice with 5 mL of cold 5% mannitol solution. Metabolic activity was rapidly quenched by adding 0.5 mL methanol containing internal standards (100 µM methionine sulfone and camphor 10-sulfonic acid). Intracellular metabolites were extracted using a solvent extraction method by mixing homogenates with 400 µL chloroform and 200 µL Milli-Q water. The mixture was centrifuged (5000 rpm, 4°C, 5 min). Subsequently, the aqueous layer was filtered using 5-kDa cut-off filters (Millipore, Bedford, MA) and centrifuged (10,000 rpm, 4°C, 6 h). The filtrate was dried using a vacuum evaporator

(4000 rpm, 4°C, 4 h) and reconstituted in 50 µL Milli-Q water containing spiked internal standards (25 mM each of 3-aminopyrrolidine and trimesic acid) before analysis.

CE-TOF/MS was performed using an Agilent CE Capillary Electrophoresis System coupled with an Agilent 6210 Time-of-Flight mass spectrometer (Agilent Technologies, Palo Alto, CA) as described by Human Metabolome Technologies, Inc. (HMT, Tsuruoka, Japan) (52).

Bacterial metabolite contamination testing

Since *V. parahaemolyticus* can adhere to the host cell surface during the coculture mammalian period, thus bacterially derived metabolites can be co-extracted with the host's metabolites. We determined that after two washing cycles with 5 mL of 5% mannitol solution, the number of *V. parahaemolyticus* adhered in Caco-2 cells was approximately 1×10^5 bacterial cells per sample. Still, we were unable to detect significant bacteria-derived metabolites in 1×10^7 bacterial cells/mL in our CE-TOF/MS analysis. It suggests that bacterial-derived metabolite contamination was negligible comparing to host-derived metabolites.

Data processing, normalization, and statistical analysis

Data processing was conducted using Mass Hunter software (Agilent Technologies, Palo Alto, CA). Metabolites are identified by matching their normalized migration times and accurate *m/z* values for each peak to the mixture of standard compounds (Human Metabolome Technologies, Inc. HMT, Tsuruoka, Japan). Metabolite's peak area values were normalized by median centering. Missing values were replaced by the lowest value detected for that specific metabolite. Statistical analysis of fold changes by two-way ANOVA and Dunnett's multiple comparison tests were used to determine metabolites with a significant alteration ($p \leq 0.05$) for each group of samples infected by a different *V. parahaemolyticus* strain. Statistical analysis was performed using GraphPad Prism 8 (GraphPad Software, USA). Multivariate statistical analysis, hierarchical clustering by heatmap and PCA of metabolite's dataset were computed using the Web-based MetaboAnalyst suite (26). Metabolite Set Enrichment Analysis (MSEA) was performed using MetaboAnalyst 4.0. Data for metabolites detected in each sample groups were input into MSEA with annotation based on standard chemical names. Metabolites were confirmed manually using Human Metabolome Database (HMDB) and human reference pathway library was used for the pathway enrichment analysis (KEGG Database).

Cytotoxicity assay

The cytotoxicity assay used a quantitative measurement of lactate dehydrogenase (LDH) release in the culture medium. In brief, the supernatants of infected cells or treatments were collected at corresponding post-infection points, and lactate dehydrogenase (LDH) release was measured with a Non-Radioactive Cytotoxicity Assay (Promega, Madison, WI) according to the manufacturer's manual. Fifty microliters of cell culture supernatant were transferred into a transparent 96-well plate, and 50 μL of assay buffer was added and then incubated at room temperature in the dark for 30 min. The reaction was stopped by the addition of 50 μL of 1 M stop buffer. LDH release was quantified by measuring absorbance at 490 nm.

Glutathione measurement

Total glutathione was determined using a Glutathione Quantification Kit (Dojindo Molecular Technologies, Inc.) according to the manufacturer's instructions. In brief, in six-well plates, Caco-2 cells infected with *V. parahaemolyticus* strains were washed twice with 2 mL of PBS. The cells were then lysed by the addition of 300 μL of 10 mM HCl and then frozen and thawed twice, and then, the samples were centrifuged at 12,000 rpm for 10 min. The supernatant was used for a GSH assay, and the absorbance at 405 nm was measured.

Reactive oxygen species measurement

Cells (10^4/well) were seeded in 96-well plates for 4 days. Cells were infected with different strains of *V. parahaemolyticus* for respective periods with an MOI of 50:1. After removal of the culture medium, the level of hydroperoxide was measured by incubating with 5 µM BES-H_2O_2-AM and 2.5 µM Bes-SO-AM (Wako Chemicals, Osaka, Japan) at 37°C for 1 h. After washing twice with PBS, the BES-H_2O_2-AM and Bes-SO-AM fluorescent signals were detected at excitation/emission wavelengths of 485/530 and 505/544 nm, respectively.

PFK activity measurement

The phosphofructokinase activity was measured using the phosphofructokinase (PFK) Activity Colorimetric Assay Kit (BioVision, Inc., USA) according to the manufacturer's instructions.

Funding

This study was financially supported by a grant-in-aid for scientific research from JSPS Kakenhi (grant number JP 25750043). Nguyen Quoc Anh was supported by The Japanese Government (MEXT) Scholarship (ID number: 153958)

Acknowledgments

Metabolomics analysis platform was supported by the Support Center for The Special Mission Center for Metabolome Analysis, School of Medical Nutrition, Faculty of Medicine of Tokushima University. We are thankful to the Support Center for Advanced Medical Sciences, Institute of Biomedical Sciences, and Tokushima University Graduate School for providing research materials.

Our special thanks to Dr. Le Danh Tuyen (NIN), Ms. Rumiko Masuda, and Ms. Yumi Harada for their critical inputs.

The authors would like to thank enago (www.enago.jp/) for the English language review.

References

1. Ahmad A, Brumble L, Maniaci M. 2013. *Vibrio parahaemolyticus* Induced Necrotizing Fasciitis: An Atypical Organism Causing an Unusual Presentation. Case Rep Infect Dis 2013:216854.
2. Daniels NA, MacKinnon L, Bishop R, Altekruse S, Ray B, Hammond RM, Thompson S, Wilson S, Bean NH, Griffin PM, Slutsker L. 2000. *Vibrio parahaemolyticus* infections in the United States, 1973-1998. J Infect Dis 181:1661–1666.
3. Li J, Xue F, Yang Z, Zhang X, Zeng D, Chao G, Jiang Y, Li B. 2016. *Vibrio parahaemolyticus* Strains of Pandemic Serotypes Identified from Clinical and Environmental Samples from Jiangsu, China. Front Microbiol 7:787.
4. Vezzulli L, Grande C, Reid PC, Hélaouët P, Edwards M, Höfle MG, Brettar I, Colwell RR, Pruzzo C. 2016. Climate influence on Vibrio and associated human diseases during the past half-century in the coastal North Atlantic. Proc Natl Acad Sci USA 113:E5062–E5071.
5. Jones JL, Lüdeke CH, Bowers JC, Garrett N, Fischer M, Parsons MB, Bopp CA, DePaola A. 2012. Biochemical, Serological, and Virulence Characterization of Clinical and Oyster *Vibrio parahaemolyticus* Isolates. J Clin Microbiol 50:2343–2352.
6. O'Boyle N, Boyd A. 2014. Manipulation of Intestinal Epithelial Cell Function by the Cell Contact-Dependent Type III Secretion Systems of Vibrio Parahaemolyticus. Front Cell Infect Microbiol 3:114.
7. Makino K, Oshima K, Kurokawa K, Yokoyama K, Uda T, Tagomori K, Iijima Y, Najima M, Nakano M, Yamashita A, Kubota Y, Kimura S, Yasunaga T, Honda T, Shinagawa H,

Hattori M, Iida T. 2003. Genome sequence of *Vibrio parahaemolyticus*: a pathogenic mechanism distinct from that of *V cholerae*. Lancet 361:743–749.

8. Hurley CC, Quirke A, Reen FJ, Boyd EF. 2006. Four Genomic Islands That Mark Post-1995 Pandemic *Vibrio Parahaemolyticus* Isolates. BMC Genomics 7:104.
9. Boyd EF, Cohen AL, Naughton LM, Ussery DW, Binnewies TT, Stine OC, Parent MA. 2009. Molecular Analysis of the Emergence of Pandemic *Vibrio parahaemolyticus*. BMC Microbiology 8:110.
10. Hiyoshi H, Kodama T, Iida T, Honda T. 2010. Contribution of *Vibrio parahaemolyticus* virulence factors to cytotoxicity, enterotoxicity, and lethality in mice. Infect Immun 78:1772–1780.
11. Piñeyro P, Zhou X, Orfe LH, Friel PJ, Lahmers K, Call DR. 2010. Development of Two Animal Models To Study the Function of *Vibrio Parahaemolyticus* Type III Secretion Systems. Infect Immun 78:4551–4559.
12. Ritchie JM, Rui H, Zhou X, Iida T, Kodoma T, Ito S, Davis BM, Bronson RT, Waldor MK. 2012. Inflammation and Disintegration of Intestinal Villi in an Experimental Model for *Vibrio parahaemolyticus*-Induced Diarrhea. PLoS Pathog 8:e1002593.
13. Yang H, de Souza Santos M, Lee J, Law HT, Chimalapati S, Verdu EF, Orth K, Vallance BA. 2019. A Novel Mouse Model of Enteric *Vibrio Parahaemolyticus* Infection Reveals That the Type III Secretion System 2 Effector VopC Plays a Key Role in Tissue Invasion and Gastroenteritis. MBio 10:e02608-19.
14. Letchumanan V, Chan KG, Lee LH. 2014. *Vibrio parahaemolyticus*: a review on the pathogenesis, prevalence, and advance molecular identification techniques. Front Microbiol 5:705.

15. Ono T, Park KS, Ueta M, Iida T, Honda T. 2006. Identification of proteins secreted via *Vibrio parahaemolyticus* type III secretion system 1. Infect Immun. 74:1032–1042.

16. Zhou X, Konkel ME, Call DR. 2009. Type III secretion system 1 of *Vibrio parahaemolyticus* induces oncosis in both epithelial and monocytic cell lines. Microbiology 155:837–851.

17. Shimohata T, Nakano M, Lian X, Shigeyama T, Iba H, Hamamoto A, Yoshida M, Harada N, Yamamoto H, Yamato M, Mawatari K, Tamaki T, Nakaya Y, Takahashi A. 2011. *Vibrio parahaemolyticus* infection induces modulation of IL-8 secretion through dual pathway via VP1680 in Caco-2 cells. J Infect Dis 203:537–544.

18. Matlawska-Wasowska K, Finn R, Mustel A, O'Byrne CP, Baird AW, Coffey ET, Boyd A. 2010. The *Vibrio parahaemolyticus* Type III Secretion Systems Manipulate Host Cell MAPK for Critical Steps in Pathogenesis. BMC Microbiol 10: 329.

19. Higa N, Toma C, Koizumi Y, Nakasone N, Nohara T, Masumoto J, Kodama T, Iida T, Suzuki T. 2013. *Vibrio parahaemolyticus* effector proteins suppress inflammasome activation by interfering with host autophagy signaling. PLoS Pathog 9:e1003142.

20. Matsuda S, Okada N, Kodama T, Honda T, Iida T. 2012. A Cytotoxic Type III Secretion Effector of *Vibrio parahaemolyticus* Targets Vacuolar H+-ATPase Subunit c and Ruptures Host Cell Lysosomes. PLoS Pathog 8:e1002803.

21. Sreelatha A, Bennett TL, Zheng H, Jiang QX, Orth K, Starai VJ. 2013. Vibrio effector protein, VopQ, forms a lysosomal gated channel that disrupts host ion homeostasis and autophagic flux. Proc Natl Acad Sci USA 110:11559–11564.

22. Sreelatha A, Bennett TL, Carpinone EM, O'Brien KM, Jordan KD, Burdette DL, Orth K, Starai VJ. 2015. Vibrio effector protein VopQ inhibits fusion of V-ATPase–containing membranes. Proc Natl Acad Sci USA 112:100–105.

23. De Nisco NJ, Kanchwala M, Li P, Fernandez J, Xing C, Orth K. 2017. Cytotoxic Vibrio T3SS1 Rewires Host Gene Expression to Subvert Cell Death Signaling and Activate Cell Survival Networks. Sci Signal 10:eaal4501.

24. Nguyen CT, Shetty V, Maresso AW. 2015. Global metabolomic analysis of a mammalian host infected with bacillus anthracis. Infect Immun 83:4811–4825.

25. Pacchiarotta T, Deelder AM, Mayboroda OA. 2012. Metabolomic investigations of human infections. Bioanalysis 4:919–925.

26. Chong J, Soufan O, Li C, Caraus I, Li S, Bourque G, Wishart DS, Xia J. 2018. MetaboAnalyst 4.0: Towards more transparent and integrative metabolomics analysis. Nucl Acids Res 46:W486–W494.

27. Mor I, Cheung EC, Vousden KH. 2011. Control of glycolysis through regulation of PFK1: Old friends and recent additions. Cold Spring Harb Symp Quant Biol 76:211–216.

28. Williams NC, O'Neill LAJ. 2018. A Role for the Krebs Cycle Intermediate Citrate in Metabolic Reprogramming in Innate Immunity and Inflammation. Front Immunol 9:141.

29. Fink MP. 2007. Ethyl Pyruvate: A Novel Anti-Inflammatory Agent. J Intern Med 261:349–362.

30. Shen H, Hu X, Liu C, Wang S, Zhang W, Gao H, Stetler RA, Gao Y, Chen J. 2010. Ethyl Pyruvate Protects against Hypoxic-Ischemic Brain Injury via Anti-Cell Death and Anti-Inflammatory Mechanisms. Neurobiol Dis 37:711–722.

31. JanssenDuijghuijsen LM, Grefte S, de Boer VCJ, Zeper L, van Dartel DAM, van der Stelt I, Bekkenkamp-Grovenstein M, van Norren K, Wichers HJ, Keijer J. 2017. Mitochondrial ATP Depletion Disrupts Caco-2 Monolayer Integrity and Internalizes Claudin 7. Front Physiol 8:794.

32. Aguer C, Gambarotta D, Mailloux RJ, Moffat C, Dent R, McPherson R, Harper ME. 2011. Galactose enhances oxidative metabolism and reveals mitochondrial dysfunction in human primary muscle cells. PLoS One 6:e28536.

33. Priscilla KN. 2019. Metabolism as a driver of immune response. Science 363:137–39.

34. Neagu M, Constantin C, Popescu ID, Zipeto D, Tzanakakis GN, Nikitovic D, Fenga C, Stratakis C, Spandidos DA, Tsatsakis AM. 2019. Inflammation and metabolism in cancer cell—mitochondria key player. Front Oncol 9:348.

35. Yang, Qiuli, Ruichen Liu, Qing Yu, Yujing Bi, and Guangwei Liu. 2019. "Metabolic Regulation of Inflammasomes in Inflammation." Immunology 157, no. 2: 95–109.

36. Moon JS, Hisata S, Park MA, DeNicola GM, Ryter SW, Nakahira K, Choi AM. 2015. MTORC1-Induced HK1-Dependent Glycolysis Regulates NLRP3 Inflammasome Activation. Cell Rep 12:102–115.

37. Xie M, Yu Y, Kang R, Zhu S, Yang L, Zeng L, Sun X, Yang M, Billiar TR, Wang H, Cao L, Jiang J, Tang D. 2016. PKM2-Dependent Glycolysis Promotes NLRP3 and AIM2 Inflammasome Activation. Nat Commun 7:13280.

38. Sanman LE, Qian Y, Eisele NA, Ng TM, van der Linden WA, Monack DM, Weerapana E, Bogyo M.. 2016. Disruption of glycolytic flux is a signal for inflammasome signaling and pyroptotic cell death. ELife 5:e13663.

39. Nomura J, So A, Tamura M, Busso N. 2015. Intracellular ATP decrease mediates NLRP3 inflammasome activation upon nigericin and crystal stimulation. J Immunol 195:5718–5724.

40. Wynosky-Dolfi MA, Snyder AG, Philip NH, Doonan PJ, Poffenberger MC, Avizonis D, Zwack EE, Riblett AM, Hu B, Strowig T, Flavell RA. 2014. Oxidative metabolism enables salmonella evasion of the NLRP3 inflammasome. J Exp Med 211:653–668.

41. Ren W, Rajendran R, Zhao Y, Tan B, Wu G, Bazer FW, Zhu G, Peng Y, Huang X, Deng J, Yin Y. 2018. Amino acids as mediators of metabolic cross talk between host and pathogen. Front Immunol 9:318.

42. Liew KL, Jee JM, Yap I, Yong PV. 2016. In vitro analysis of metabolites secreted during infection of lung epithelial cells by Cryptococcus neoformans. PLoS One 4:e0153356

43. Ren W, Yin J, Xiao H, Chen S, Liu G, Tan B, Li N, Peng Y, Li T, Zeng B, Li W. 2016. Intestinal microbiota-derived GABA mediates interleukin-17 expression during enterotoxigenic Escherichia coli infection. Front Immunol 7:685.

44. Tattoli I, Sorbara MT, Vuckovic D, Ling A, Soares F, Carneiro LA, Yang C, Emili A, Philpott DJ, Girardin SE. 2012. Amino acid starvation induced by invasive bacterial pathogens triggers an innate host defense program. Cell Host Microbe 11:563–575.

45. Burdette DL, Seemann J, Orth K. 2009. Vibrio VopQ induces PI3-kinase-independent autophagy and antagonizes phagocytosis. Mol Microbiol 73:639–649.

46. Gerald L. 2018. Chapter 4-Proteins. *In* Human Biochemistry, edited by Gerald Litwack, 63–94. Academic Press, Boston.

47. Shelly LC. 2013. Glutathione synthesis. Biochimica Et Biophysica Acta 1830:3143–3153.

48. Meister A. 1992. Biosynthesis and function of glutathione, an essential biofactor. J Nutrit Sci Vitaminol 38:1–6.

49. Liu Y, Hyde AS, Simpson MA, Barycki JJ. 2014. Emerging regulatory paradigms in glutathione metabolism. Adv Cancer Res 122:69–101.

50. Forman HJ, Zhang H, Rinna A. 2009. Glutathione: Overview of its protective roles, measurement, and biosynthesis. Mol Asp Med 30:1–12.

51. Park KS, Ono T, Rokuda M, Jang MH, Okada K, Iida T, Honda T. 2004. Functional Characterization of Two Type III Secretion Systems of *Vibrio parahaemolyticus*. Infect Immun 72:6659–6665.

52. Kami K, Fujimori T, Sato H, Sato M, Yamamoto H, Ohashi Y, Sugiyama N, Ishihama Y, Onozuka H, Ochiai A, Esumi H. 2013. Metabolomic profiling of lung and prostate tumor tissues by capillary electrophoresis time-of-flight mass spectrometry. Metabolomics 9:444–453.

53. Nomura T, Hamashima H, Okamoto K. 2000. Carboxy terminal region of haemolysin of *Aeromonas sobria* triggers dimerization. Microb Pathog 28:25–36.

Table 1. Strains and plasmids used in this study

Strains or plasmid	Genotype	**Description**	Source or reference
V. parahaemolyticus strains			
RIMD2210633	Wildtype	Clinical isolate; KP positive, serotype O3: K6	(8)
vscN1-vscN2	Δ vscN1, Δ vscN2	T3SS1 and T3SS2 deficient strain: *vscN1* and *vscN2* encoding a cytoplasmic protein of the TTSS apparatus deletion mutant derived from Wildtype strain	(51)
POR2	Δ *tdhAS*, Δ vscD1	TDH toxin and T3SS1 deficient strain: *vcrD1* needle apparatus gene deletion from POR-1 strain	(51)
POR3	Δ *tdhAS*, Δ vscD2	TDH toxin and T3SS2 deficient strain: *vcrD2* needle apparatus gene deletion derived from POR-1 strain	(51)
POR4	Δ *tdhAS*, Δ vcrD1, Δ vcrD2	TDH toxin, T3SS1 and T3SS2 deficient mutant derived from POR-1 in which the T3SS1 needle apparatus gene (vcrD1) and T3SS2 needle apparatus gene (vcrD2) were deleted	(52)
ET4	Δ *tdhAS*, Δ vscD2, ΔVP1683, ΔVP1686, ΔVPA0450	VP1680 containing strain - mutant strain deleted other T3SS1 effectors: ΔVP1683, ΔVP1686, ΔVPA0450 derived from POR-3 strain	This study
S1-ENM	Δ *tdhAS*, Δ vscD2, ΔVP1680, ΔVP1683, ΔVP1686, ΔVPA0450	T3SS1 effector deficient strain, mutant strain deleted all T3SS1 effectors: ΔVP1680, ΔVP1683, ΔVP1686, ΔVPA0450 derived from POR-3 strain	This study
E. coli			
SM10 λpir	thi thr leu tonA lacY supE recA::RP4-2Tc::Mu λpir R6K	Plasmid mobilization strain	Lab Collection
DH5α		TOPO sub-cloning	Lab Collection
Plasmid			
pYAK		R6K-ori suicide vector, containing sacB gene for counterselection, Cm^r	(51)
$pSA19CP^r$		Complement vector for V. parahaemolyticus	(53)
pSA-vp1680		Complement vector, expressing the open reading frame of vp1680 gene controlled by a tdhA promoter Cm^r	This study

Cm^r, chloramphenicol resistant

Table 2. The phenotype of *V. parahaemolyticus* strains derived from the RIMD2210633 clinical isolate used in this study

Strain	TDH	T3SS1				T3SS2
		VopQ	*VopR*	*VopS*	*VPA0450*	
RIMD2210633	+	+	+	+	+	+
vscN1-vscN2	+	-	-	-	-	-
POR2	-	-	-	-	-	+
POR3	-	+	+	+	+	-
POR4	-	-	-	-	-	-
ET4	-	+	-	-	-	-
S1-ENM	-	-	-	-	-	-

Figure Legends

Figure 1. Multivariate analyses revealed a specific signature for *Vibrio parahaemolyticus* infection associated with T3SS1. Metabolites were extracted from Caco-2 cells infected with different *V. parahaemolyticus strains* at 120 min post-infection (MOI = 50:1; $n = 4$). **(A)** Heatmap and hierarchical clustering of Caco-2 metabolomes according to the infection strains and metabolite abundances showing the differences and similarities of Caco-2 cells metabolic states when infected with V. *parahaemolyticus* strains. The metabolite abundances were scaled on a range of −1.5 to 1.5 and clustered according to Euclidean distance. **(B)** Three-dimensional (3D) principal component analysis (PCA) score plots showed distinct clusterization of Caco-2 cell metabolites infected with the control group (sham infection); POR4, ΔvscN1-ΔvscN2; POR2; POR3; and wild type (WT). **(C)** Metabolite set enrichment analysis (MSEA) showed 20 significantly enriched biological pathways ($p < 0.05$) associated with *V. parahaemolyticus* infection. Color intensity (white to red) indicates the increasing statistical significance of pathway enrichment analysis. The graph was plotted on the y-axis showed the −log of p-values from pathway enrichment analysis and on the x-axis from pathway topology analysis.

Figure 2. Multivariate analyses showed a specific metabolic signature associated with VopQ. Metabolite extracted from Caco-2 cells infected with different S1-ENM and ET4 strains at 90 post-infection (MOI = 50:1; $n = 4$). **(A)** Heatmap and hierarchical clustering of Caco-2 metabolomes according to the infection strains and metabolite abundances showing the similarities of Caco-2 cells metabolic states when infected with POR3 and ET4 strains compared

to S1-ENM and control. The metabolite abundances were scaled on a range of −1.5 to 1.5 and clustered according to Euclidean distance. **(B)** Three-dimensional (3D) principal component analysis (PCA) score plots showed distinct clusterization of Caco-2 cell metabolites infected with POR3 and ET4 compared with the control group (sham infection) and S1-ENM. **(C)** Hierarchical clustering analysis was performed according to Euclidean distance between the control group (sham infection); POR3, ET4, and S1-ENM showed two district clusterization.

Figure 3. VopQ rerouted Caco-2 cell metabolites from glycolysis to PPP metabolites. The relative abundances of glycolytic and PPP metabolites of Caco-2 cells infected with different *V. parahaemolyticus* mutants extracted 90 min post-infection. Mean ± SD is shown for 4 biological replicates. One-way ANOVA with Dunnett's multiple comparison test was applied to the S1-ENM, ET4, and POR3 groups for comparison to the control group (*$p < 0.05$; **$p < 0.01$). The y-axis represents the relative ambulance in peak intensity (concentration) of the identified metabolites. The black, blue, and highlighted blue letters represent the metabolic intermediates from glycolysis, pentose phosphate pathway, and TCA cycle, respectively. The green and orange letters signify enzymes and co-factors that catalyze the corresponding metabolic pathways.

Figure 4. VopQ disrupted cellular biogenetics. **(A)** The relative abundances of ATP, ADP, and AMP metabolites of Caco-2 cells infected with different V. *parahaemolyticus* mutants measured by CE-MS at 90 min post-infection. Mean ± SD is shown for four biological replicates. One-way ANOVA with Dunnett's multiple comparison test was applied to S1-ENM, ET4, and POR3 groups for comparisons to the control group (*$p < 0.05$; **$p < 0.01$). Caco-2 cell cytotoxicity at 4 h with different *V. parahaemolyticus* mutants measured by LDH release assay. Caco-2 cells

were treated with **(B)** 25 mM of 2-deoxyglucose (2-DG) and **(C)** 50 nM rotenone. Statistical analysis by Student's *t*-test (*$p < 0.05$ or **$p < 0.01$) with mean ± SD shown for three biological replicates.

Figure 5. VopQ disrupted cellular amino acid hemostasis. **(A)** The percent relative abundances of amino acids of Caco-2 cells infected with different *V. parahaemolyticus* mutants measured by CE-MS at 90 min post-infection. Mean ± SD shown for four biological replicates. One-way ANOVA with Dunnett's multiple comparison test was applied to the S1-ENM, ET4, and POR3 groups for comparisons to the control group (*$p < 0.05$ or **$p < 0.01$). **(B), (C)** Cellular glutathione and glutathione disulfide (GSSG) concentration of Caco-2 cells infected with different *V. parahaemolyticus* mutants for 2 h. **(D), (E)** Relative level of hydrogen peroxide (H_2O_2) and superoxide (O_2^-) of Caco-2 cells infected with different *V. parahaemolyticus* mutants for 2 h. Statistical analysis by One-way ANOVA with Dunnett's multiple comparison test was applied to the S1-ENM, ET4, and POR3 groups for comparisons to the control group for 4 biological replications (*$p < 0.05$ or **$p < 0.01$).

Supplemental Material

Table S1. Primers list used in this study

Figure S1. **(A)** Metabolomics analysis workflow of Caco-2 cells infected with Vibrio *parahaemolyticus* strains. **(B)** Cytotoxic activity (% LDH release) of Caco-2 cells infected with different Vibrio *parahaemolyticus* strains for WT or the isogenic mutants at a multiplicity of infection (MOI) = 50:1 at 3-hour post-infection. **(C)** Cell viability (Trypan blue exclusion staining) of Caco-2 cells infected with different Vibrio *parahaemolyticus* strains for WT or the isogenic mutants at a multiplicity of infection (MOI) = 50:1 at 3-hour post-infection. The strains tested were WT (RIMD2210633), POR2 (Δ *tdhAS*, Δ vscD1), POR3(Δ *tdhAS*, Δ vscD2), vscN1-vscN2 (ΔvscN1-ΔvscN2) and POR4 (Δ *tdhAS*, Δ vscD1, Δ vscD2). The error bars indicate standard deviations from triplicate samples (n=3).

Figure S2. Multivariate analyses showed a specific metabolic signature associated with VopQ. Metabolite extracted from Caco-2 cells infected with different S1-ENM and ET4 strains at 45-minute, 90 minute and 150-minute post-infection (MOI = 50; n = 3). Heatmap and hierarchical clustering of Caco-2 metabolomes according to the metabolite abundances between control (sham infection); S1-ENM and ET4, showing the differences and similarities of the Caco-2 cells metabolic pattern at different time points. The metabolite abundances were scaled in a range of − 3 to 3 and clustered according to the Euclidian distance matrix.

Figure S3. Multivariate analyses showed the VP1680 effector repressed INT-407 cells central metabolism. Metabolite extracted from INT-407 cells infected with different V. *parahaemolyticus* strains at 90-min post-infection (MOI = 10:1; n = 4). Heatmap represented hierarchical clustering analysis with significantly relative metabolite abundances between control (sham infection), S1-ENM, and ET4. The metabolite abundances were scaled in a range of − 3 to 3 and clustered according to the Euclidean distance matrix.

Figure S4. Relative phosphofructokinase activities of Caco-2 cell infected with POR3, ET4, S1-ENM strains, and control extracted at 2-hour post-infection. No significant difference detected by One-way ANOVA with Dunnett's multiple comparison test was applied to the S1-ENM, ET4, and POR3 groups for comparison to the control group (n = 4).

Figure S5. Caco-2 cells were cultured in the high glucose medium DMEM (4.5 mg/l glucose) for 4 days. For glucose-free medium culture, cells after reaching the confluence medium contain glucose were replaced with Glucose free DMEM medium for 1 day before the experiment. For the galactose medium culture, Caco-2 cells were cultured in galactose medium for 4 passages in 20 days. The fifth cell passage was selected for the experiment. Cytotoxicity of Caco-2 cells infected with different V. *parahaemolyticus* strains with treatments: 4.5 g/ml DMEM medium, glucose-free medium, 4.5 mg/l galactose medium for 4 hours. Mean ± SD shown for 4 biological replicates. Student t-test was performed for pair comparison for treatments in each group (*p<0.01).

Figure S6. Effects of Glycine and NAC on the GSH level. Caco-2 cells were incubated with 0.5 mmol/l Glycine or/and 0.5 mmol/l NAC for 8 hours prior to starting an infection. GSH content was measured by colorimetric assay at 3 hour-post infections. Results were expressed as mean, and SD were calculated from 4 biological replications. No significant differences found by One-way ANOVA with Dunnett's multiple comparison test between treatments with ET4 infection.

Figure S7. Effects of ethyl pyruvate on ATP level and cell cytotoxicity on Caco-2 cells. Caco-2 cells were incubated with 5 mM and 10 mM of Ethyl pyruvate for 2 hours before and continuously during the infection (MOI) = 50:1 with POR3. **(A)** Cellular ATP content was measured by a luciferase assay at 2 hour-post-infections. **(B)** Cytotoxic activity (% LDH release) of Caco-2 cells at 6-hour post-infection. Results were expressed as mean, and SD was calculated from 4 biological replications. No significant differences found by One-way ANOVA with Dunnett's multiple comparison test between treatments with POR3 infection.

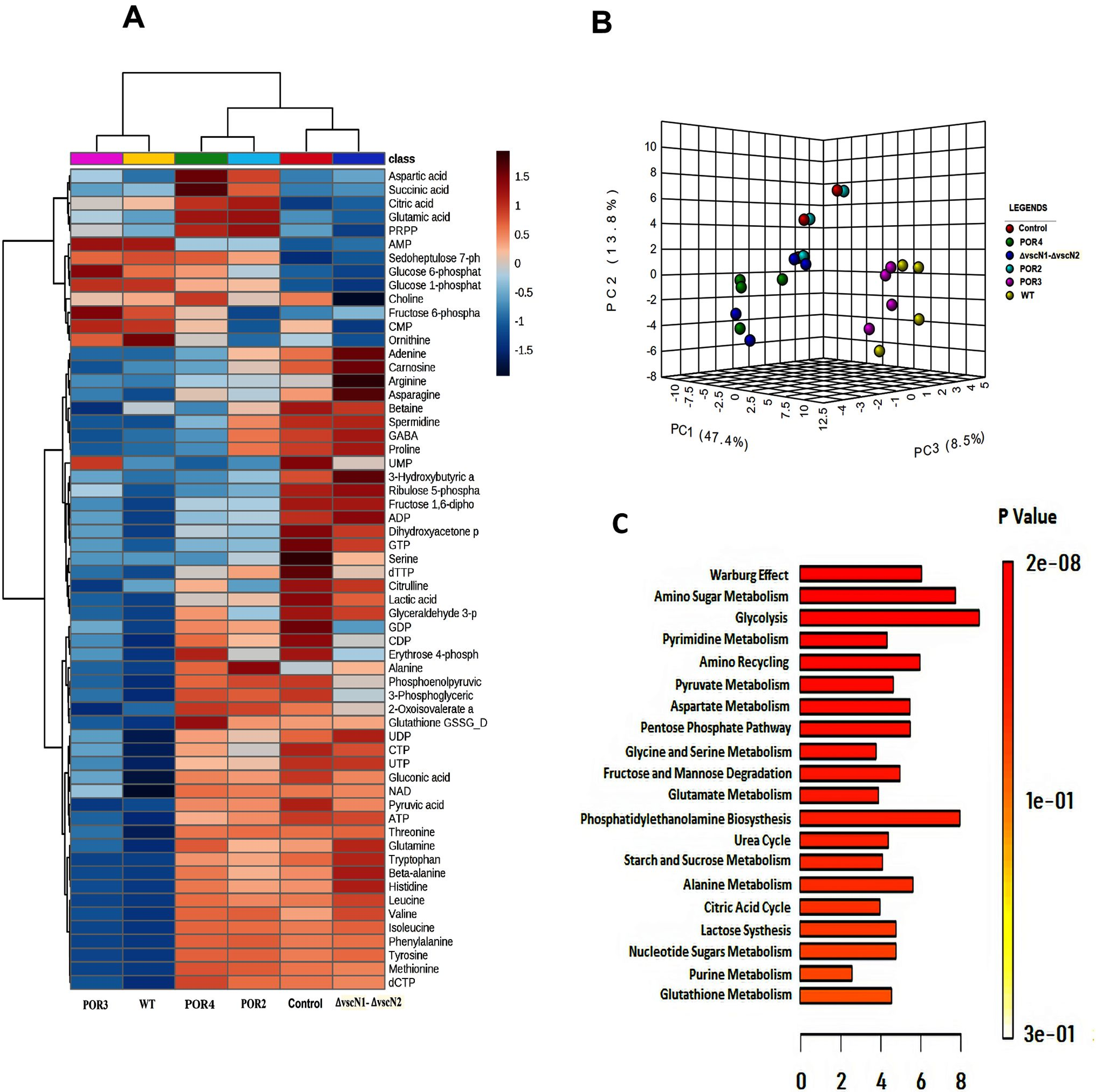

A
class
Aspartic acid
Succinic acid
Citric acid
Glutamic acid
PRPP
AMP
Sedoheptulose 7-ph
Glucose 6-phosphat
Glucose 1-phosphat
Choline
Fructose 6-phospha
CMP
Ornithine
Adenine
Carnosine
Arginine
Asparagine
Betaine
Spermidine
GABA
Proline
UMP
3-Hydroxybutyric a
Ribulose 5-phospha
Fructose 1,6-dipho
ADP
Dihydroxyacetone p
GTP
Serine
dTTP
Citrulline
Lactic acid
Glyceraldehyde 3-p
GDP
CDP
Erythrose 4-phosph
Alanine
Phosphoenolpyruvic
3-Phosphoglyceric
2-Oxoisovalerate a
Glutathione GSSG_D
UDP
CTP
UTP
Gluconic acid
NAD
Pyruvic acid
ATP
Threonine
Glutamine
Tryptophan
Beta-alanine
Histidine
Leucine
Valine
Isoleucine
Phenylalanine
Tyrosine
Methionine
dCTP
1.5
1
0.5
0
-0.5
-1
-1.5
POR3
WT
POR4
POR2
Control
ΔvscN1- ΔvscN2
B
PC2 (13.8%)
PC1 (47.4%)
PC3 (8.5%)
LEGENDS
Control
POR4
ΔvscN1-ΔvscN2
POR2
POR3
WT
C
P Value
2e-08
1e-01
3e-01
Warburg Effect
Amino Sugar Metabolism
Glycolysis
Pyrimidine Metabolism
Amino Recycling
Pyruvate Metabolism
Aspartate Metabolism
Pentose Phosphate Pathway
Glycine and Serine Metabolism
Fructose and Mannose Degradation
Glutamate Metabolism
Phosphatidylethanolamine Biosynthesis
Urea Cycle
Starch and Sucrose Metabolism
Alanine Metabolism
Citric Acid Cycle
Lactose Synthesis
Nucleotide Sugars Metabolism
Purine Metabolism
Glutathione Metabolism
0
2
4
6
8

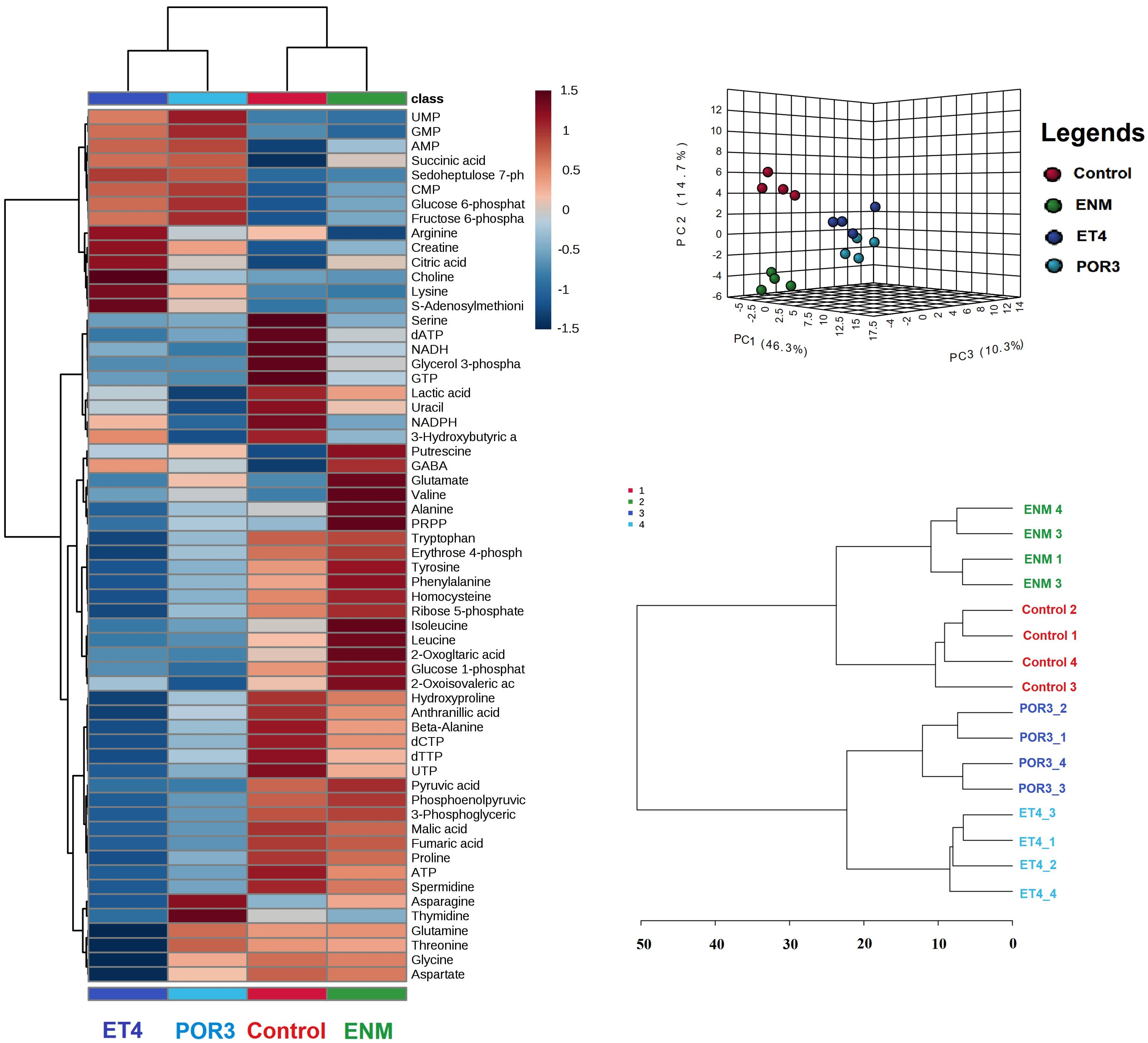

class
UMP
GMP
AMP
Succinic acid
Sedoheptulose 7-ph
CMP
Glucose 6-phosphat
Fructose 6-phospha
Arginine
Creatine
Citric acid
Choline
Lysine
S-Adenosylmethioni
Serine
dATP
NADH
Glycerol 3-phospha
GTP
Lactic acid
Uracil
NADPH
3-Hydroxybutyric a
Putrescine
GABA
Glutamate
Valine
Alanine
PRPP
Tryptophan
Erythrose 4-phosph
Tyrosine
Phenylalanine
Homocysteine
Ribose 5-phosphate
Isoleucine
Leucine
2-Oxogltaric acid
Glucose 1-phosphat
2-Oxoisovaleric ac
Hydroxyproline
Anthranillic acid
Beta-Alanine
dCTP
dTTP
UTP
Pyruvic acid
Phosphoenolpyruvic
3-Phosphoglyceric
Malic acid
Fumaric acid
Proline
ATP
Spermidine
Asparagine
Thymidine
Glutamine
Threonine
Glycine
Aspartate
1.5
1
0.5
0
-0.5
-1
-1.5
ET4
POR3
Control
ENM
PC2 (14.7%)
PC1 (46.3%)
PC3 (10.3%)
Legends
Control
ENM
ET4
POR3
1
2
3
4
ENM 4
ENM 3
ENM 1
ENM 3
Control 2
Control 1
Control 4
Control 3
POR3_2
POR3_1
POR3_4
POR3_3
ET4_3
ET4_1
ET4_2
ET4_4
50
40
30
20
10
0

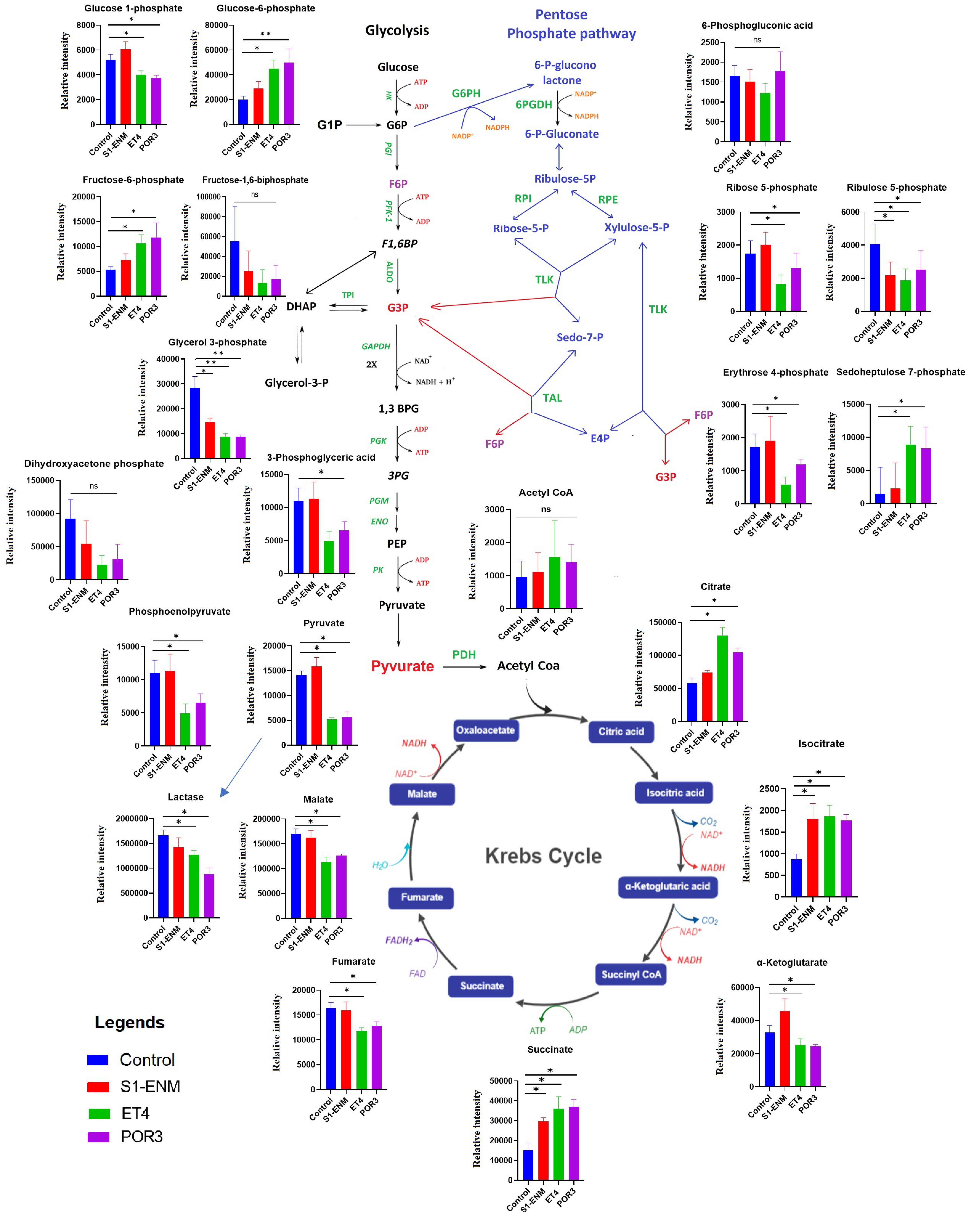
Glycolysis
Pentose
Phosphate pathway
Glucose
G1P
G6P
F6P
F1,6BP
DHAP
G3P
Glycerol-3-P
1,3 BPG
3PG
PEP
Pyruvate
Pyvurate
Acetyl Coa
PDH
HK
PGI
PFK-1
ALDO
TPI
GAPDH
PGK
PGM
ENO
PK
2X
ATP
ADP
NAD+
NADH + H+
G6PH
6PGDH
NADP+
NADPH
6-P-glucono
lactone
6-P-Gluconate
Ribulose-5P
RPI
RPE
Ribose-5-P
Xylulose-5-P
TLK
Sedo-7-P
TAL
E4P
F6P
G3P
Krebs Cycle
Oxaloacetate
Citric acid
Isocitric acid
α-Ketoglutaric acid
Succinyl CoA
Succinate
Fumarate
Malate
CO2
NAD+
NADH
FADH2
FAD
H2O
ATP
ADP
Glucose 1-phosphate
Glucose-6-phosphate
6-Phosphogluconic acid
Fructose-6-phosphate
Fructose-1,6-biphosphate
Ribose 5-phosphate
Ribulose 5-phosphate
Glycerol 3-phosphate
Erythrose 4-phosphate
Sedoheptulose 7-phosphate
Dihydroxyacetone phosphate
3-Phosphoglyceric acid
Acetyl CoA
Citrate
Phosphoenolpyruvate
Pyruvate
Isocitrate
Lactase
Malate
Fumarate
α-Ketoglutarate
Succinate
Relative intensity
Control
S1-ENM
ET4
POR3
ns
Legends
Control
S1-ENM
ET4
POR3

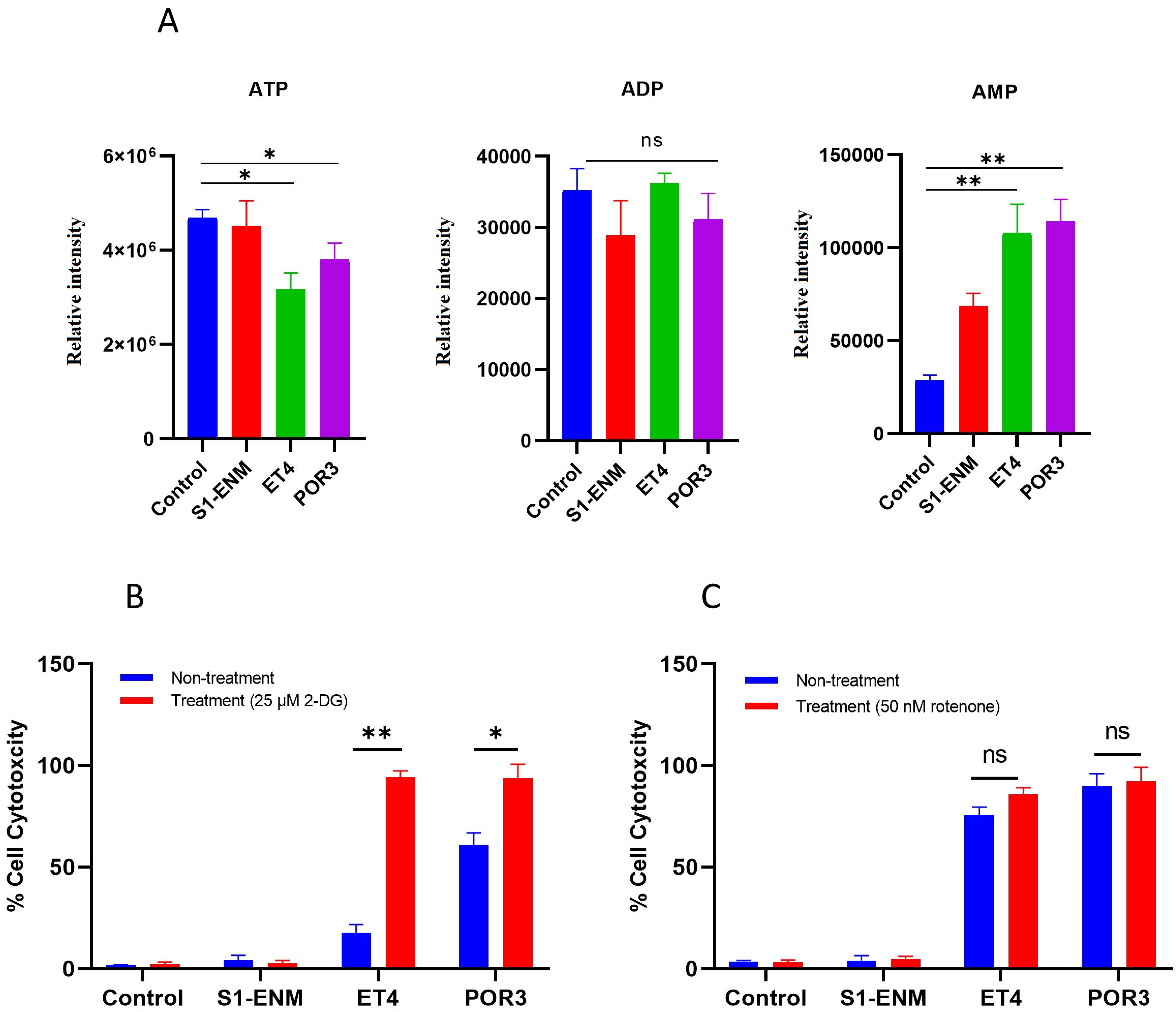
A
ATP
ADP
AMP
Relative intensity
6×10⁶
4×10⁶
2×10⁶
0
40000
30000
20000
10000
150000
100000
50000
ns
*
**
Control
S1-ENM
ET4
POR3
B
C
% Cell Cytotoxcity
150
100
50
Non-treatment
Treatment (25 μM 2-DG)
Treatment (50 nM rotenone)

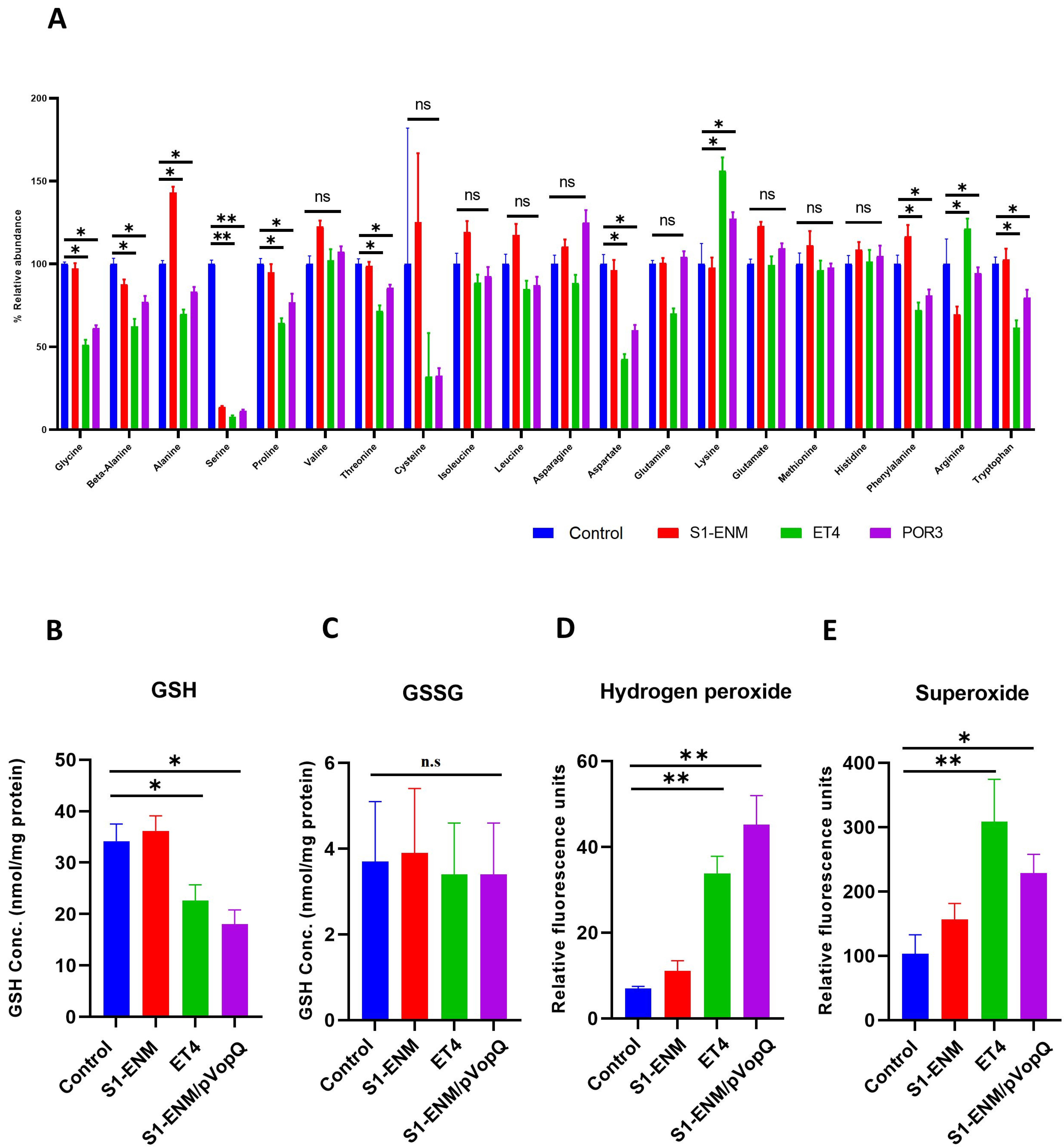
A
% Relative abundance
Glycine
Beta-Alanine
Alanine
Serine
Proline
Valine
Threonine
Cysteine
Isoleucine
Leucine
Asparagine
Aspartate
Glutamine
Lysine
Glutamate
Methionine
Histidine
Phenylalanine
Arginine
Tryptophan
Control
S1-ENM
ET4
POR3
B
GSH
GSH Conc. (nmol/mg protein)
C
GSSG
GSH Conc. (nmol/mg protein)
n.s
D
Hydrogen peroxide
Relative fluorescence units
E
Superoxide
Relative fluorescence units
Control
S1-ENM
ET4
S1-ENM/pVopQ